Synthesis and photocatalytic performance of yttrium-doped CeO$_2$ with a porous broom-like hierarchical structure

Bin Xu [a,b,c], Qitao Zhang [a,b], Saisai Yuan [a,b], Ming Zhang [a,c,**], Teruhisa Ohno [b,d,e,f,*]

[a] School of Chemistry and Chemical Engineering, Yangzhou University, Yangzhou 225002, China
[b] Department of Applied Chemistry, Faculty of Engineering, Kyushu Institute of Technology, Kitakyushu 804-8550, Japan
[c] Test Center, Yangzhou University, Yangzhou 225002, China
[d] JST, PRESTO and ACT-C, 4-1-8 Honcho Kawaguchi, Saitama 332-0012, Japan
[e] JST, ACT-C, 4-1-8 Honcho Kawaguchi, Saitama 332-0012, Japan
[f] Research Center for Advanced Eco-fitting Technology, Kyushu Institute of Technology, Tobata, Kitakyushu 804-8550, Japan

ARTICLE INFO

ABSTRACT

In this study, yttrium-doped CeO$_2$ with a broom-like porous hierarchical structure was successfully prepared by a simple template-free hydrothermal method with cerium nitrate hexahydrate and yttrium nitrate hexahydrate as original materials. Through systematic experiments, the different effects of doping concentrations on characteristics of the ceria were examined in detail and the optimal doping ratio was determined simultaneously. The morphology and element distribution of the as-prepared samples were characterized by field emission scanning electron microscopy and high-resolution transmission electron microscopy. Structure information with Rietveld refined data were obtained by using an X-ray diffractometer. Extinctive oxygen vacancy and doping oxygen vacancy were analyzed from Raman spectra. Analyses of elements and chemical valence analysis were carried out by X-ray photoelectron spectroscopy, and changes in reactive oxygen species were determined by calculation. Based on structural information, element valence states, results of hydrogen temperature-programmed reduction and oxygen temperature-programmed decomposition analysis and the results of photocatalytic decomposition of acetaldehyde, we can draw the conclusion that a certain amount of Y-doped CeO$_2$ with a broom-like porous hierarchical structure has high catalytic activity, attributed to more oxygen vacancies and surface active oxygen species generated after yttrium doping.

© 2015 Elsevier B.V. All rights reserved.

1. Introduction

Cerium dioxide, an important rare-earth oxide, has been extensively studied due to its significant fluorite-type structure, remarkable redox properties [1–3] and prominent oxygen storage and release capacity (OSC) via facile conversion between Ce^{4+} and Ce^{3+} oxidation states [2]. Ceria-based materials have been extensively utilized in many practical applications such as polishing materials [3], solar cells [4], ultraviolet blocking materials [5,6] and photocatalytic materials. Pure CeO$_2$, an n-type semiconductor, has a band gap (3.2 eV) similar to those of other commonly utilized semiconductor-based photocatalysts such as TiO$_2$ [7] and possesses potential as a suitable photocatalyst. Recently, CeO$_2$ materials with

different morphologies have been synthesized by various methods including thermal evaporation [8], coprecipitation [9], and the sol-gel technique [10]. Previous studies have indicated that excellent catalytical performance and easy functionalization of CeO$_2$ materials can been achieved by controlling their structural properties [11]. For instance, our group successfully fabricated porous broom-like CeO$_2$ [12] andCeO$_2$ with an yttrium-doped hedgehog-like 3D hierarchical structure [13]. Compared with conventional nanowires, nanorods and nanocubes as well as nanoparticles with other shapes, newly constructed CeO$_2$ with a hierarchical architecture will acquire some special properties that single morphology CeO$_2$ does not possess [10,14,15]. Although some progress has been made in the fabrication of hierarchical architectures composed of 1D nanostructures, the methods usually need special templates through a complex experimental course. For example, Mitchell et al. fabricated coral-like mesostructured CeO$_2$ using an amino acid as a template [16]. Zhong et al. reported the preparation of 3D flowerlike ceria at 180 °C with TBAB as a surfactant and EG as a solvent [17].

* Corresponding author. Fax: +81 93 884 3318.
** Corresponding author. Fax: +86 514 8797924.
E-mail addresses: lxyzhangm@yzu.edu.cn (M. Zhang), tohno@che.kyutech.ac.jp (T. Ohno).

The application of morphology and size-controlled, metal and metal oxide composites and different ionic doping are the three most commonly utilized methods for enhancing the catalytic properties of CeO_2-based materials. The keypoint in these approaches is changing the oxygen vacancy concentrations of products, because oxygen vacancies can act as electron or hole capture centers and can trap the photogenerated electrons or holes excited by ultraviolet or visible light. Oxygen vacancies can also effectively restrain the recombination of electron-hole pairs, resulting in improvement of photocatalytic activities [18]. Application of more than two or all of the above methods to the preparation of a 3D hierarchical structure of CeO_2 with a high concentration of oxygen vacancies would be a huge challenge. To the best of our knowledge, there has been no report about CeO_2 with an yttrium-doped hierarchical structure obtained by facile controlled synthesis.

Herein, we report for the first time a facile and feasible approach to prepare porous CeO_2 with a yttrium-doped broom-like hierarchical structure by a simple template-free hydrothermal technique using the simple inorganic salts $Ce(NO_3)_3$, $Y(NO_3)_3$ and the morphology-decorated agent dihydrate trisodium citrate($C_6H_5Na_3O_7\cdot2H_2O$) as original materials. Changes in the concentration of oxygen vacancies, active oxygen species on the crystal surface and tervalence cerium in the lattice, caused by variation in the amount of the yttrium dopant, are discussed in detail in this article. Meanwhile, the corresponding catalytic performance characterized by TPR and TPD exhaustively.

2. Experiment section

2.1. Materials

Dihydrate trisodium citrate ($C_6H_5Na_3O_7\cdot2H_2O$), urea, cerium nitrate hexahydrate ($Ce(NO_3)_3\cdot6H_2O$) and yttrium nitrate hexahydrate ($Y(NO_3)_3\cdot6H_2O$) were of analytical grade and used without any further purification. All of the above original materials were purchased from Wako Co., Ltd.

2.2. Preparation

A typical synthetic procedure is as follows, and the optimal synthesis conditions were described in our previous report [12]. First, 5.88 g dihydrate trisodium citrate ($C_6H_5Na_3O_7\cdot2H_2O$) was dissolved in 80 ml deionized water with vigorous magnetic stirring at room temperature. Ten minutes later, 2.4 g urea was added to the solution. The homogeneous mixture was prepared for further use. At the same time, 1.63 g cerium nitrate hexahydrate ($Ce(NO_3)_3\cdot6H_2O$) and 0.072 g,0.144 g, 0.288 g, 0.432 g or 0.575 g yttrium nitrate hexahydrate were dissolved in 20 ml deionized water with vigorous magnetic stirring at room temperature. Then each of these cerium and yttrium nitrate aqueous solutions was dropped into the above mixture at 1 ml/min, and the mixture was stirred for 30 min until the solution changed to a faint yellow color. The mixed solution was then sealed in a 100 ml Teflon-lined autoclave and heated at 120 °C for 39 h. After cooling to room temperature naturally, a white precipitate was collected by centrifugation and washed with deionized water and ethanol respectively at least three times. Yttrium-doped ceria was obtained by calcination of the as-prepared precursor in air at 500 °C for 4 h.

2.3. Characterizations

Morphology and size of the products were observed by an FE-SEM (Hitachi, S-4800, 15KV) and element and distribution HR-TEM (FEI, Tecnai G2 F30 S-TWIN, 300KV). XRD patterns of the products were obtained on a Bruker-AXS X-ray equipped with graphite monochromator and CuKa radiation ($\lambda = 1.5406$ Å). The crystallite parameters and size were calculated by the Rietveld method (TOPAS 4.0). Raman analysis (Renishaw, In via) was performed using a 532 nm excitation laser with 5 mW and an air-cooled CCD detector. Raman peak shifts were determined by fitting with the Lorentzian and Gaussian composite function. An X-ray photoelectron spectroscopy (XPS) experiment was carried on a Shimadzu KRATOS AXIS-NOVA system at room temperature under 10^{-9} pa using Al Kα radiation and C 1s peak (83.8 eV) reference.

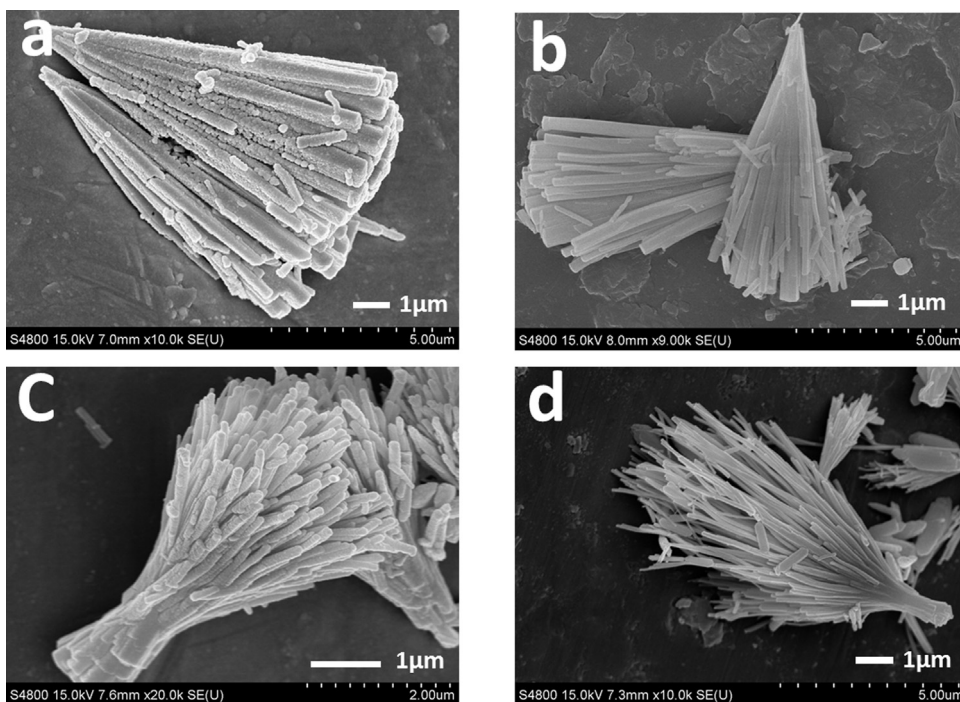**Fig. 1.** FESEM images of as-fabricated samples with different mole ratios of $Ce(NO_3)_3\cdot6H_2O$: $Y(NO_3)_3\cdot6H_2O$: (a) 1:0, (b) 1:0.1, (c) 1:0.2 and (d) 1:0.4.

Hydrogen temperature-programmed reduction (H_2-TPR) and oxygen temperature-programmed decomposition (O_2-TPD) experiments were performed on FTNESORB-3010. In each of the experiments, 500 mg was pretreated by calcination at 200 °C for 1 hour and was subsequently cooled to 100 °C under an Ar flow before being used. For the H_2-TPR experiment, the reduction process was carried out from room temperature to 900 °C under a flow of 10% H_2/Ar with 50 cm^3/min. For the O_2-TPR experiment, the adsorption of O_2 was carried out in a flow of 10% O_2/He for 1 h, followed by purging by He for 30 min for removal of residual oxygen. The consumption of H_2 or O_2 was continuously monitored by a thermal conductivity detector (TCD) operating at 60 °C and 80 mA.

2.4. Photocatalytic Evaluations.

UV lighter using black light (UVP, XX-15BLB) can be used in order to remove possible organic materials adsorbed on the surface of samples more than one week before evaluation of photocatalytic activity. The photocatalytic activity of as-fabricated samples was assessed by ability for decomposition of acetaldehyde. Ten milligrams of powder was spread on the bottom of a glass dish, and the glass dish was placed in a Tedlar bag (AS ONE Co., Ltd.). Five hundred ppm of acetaldehyde was injected into the bag together with 125 cm^3 of artificial air. Then the bag, which was fabricated above, was put into a dark place at room temperature for 2 h for the purpose of reaching an adsorption equilibrium A light-emitting diode (LED; Epitex, L365), which emitted light at wavelengths of ca. 365 nm, was used as a light source, and its intensity was controlled at 0.9 mW cm^{-2}. The concentration of generated CO_2 as s function of irradiation time was monitored by a gas chromatography (Shimadzu GC-8A, FID detector) equipped with a Porapak N-packed column and a methanizer (GL Science, MT-221).

3. Results and discussion

3.1. Morphology characterization

The morphology of as-prepared CeO_2 with different yttrium-doped concentrations was investigated by using an FE-SEM (Fig. 1) and HR-TEM (Fig. 2). Fig. 1a shows broom-like morphology CeO_2 without yttrium doping. Numerous nanorods of approximately 10 μm in length and with an average diameter of 500 nm are connected at one end and diverge at the other end to form a broom-like hierarchical architecture. Fig. 2a shows that numerous inhomogeneous ceria nanoparticles with an average range of 20 nm in diameters have loosely accumulated to form a porous broom-like morphology. Evidently, the size of these particles is inhomogeneous, and the maximum particle size may reach 40 nm while the smallest diameter is only about 10 nm. The corresponding elemental maps of products show that only Ce and O are obviously detected and well distributed throughout the individual nanorods (Fig. 1S). Furthermore, the d lattice spacing calculated from the inset image of Fig. 2a is 0.313 nm, indicating that these nanoparticles mainly expose (1 1 1) planes of a cubic fluorite structure of CeO_2.

Fig. 1b–d shows broom-like morphology of CeO_2 with yttrium doping. After doping, the morphology of the products does not change remarkably and the broom-like shape is maintained. Only changes in the surface smooth degree, averaged diameter, and length of the nanorods can be observed. With an increase in the amount of the yttrium dopant, the surface smooth degree of nanorods was obviously improved. At the same time, the length of the rods increased correspondingly. In contrast, the average diameter of the nanorods decreased greatly from 500 nm to 200 nm. Similar phenomena can be seen in the Fig. 2b–d. Numerous yttrium-doped ceria nanoparticles loosely accumulated to form a porous

broom-like morphology. However, unlike before doping, the particles sizes after doping are uniform and the average diameter is about 10 nm. As can be seen in the respective inset images, although the particles still mainly expose a (1 1 1) lattice plane of the FCC structure, the internal spacing distance increased to 0.314 nm. Fig. 3 shows corresponding elemental maps of products after yttrium doping. Not only cerium and oxygen but also yttrium are observed together, and all of these elements are well distributed throughout individual nanorods. These results suggest that yttrium has entered the lattice structure of CeO_2 and that doping is successful.

3.2. Structure characterization

X-ray diffractometer (XRD) analysis was carried out to investigate the crystal phase and purity of samples obtained with different yttrium-doped concentrations. Typical XRD patterns are shown in Fig. 4a. All of the diffraction lines could be indexed to the phase of ceria with a cubic fluorite structure (Space group: Fm–3m (2 2 5)), being in good agreement with the standard data reported in JCPDS card (No. 34-0394). The sharp diffraction peaks from all samples suggest a high degree of crystallinity of fabricated samples, and no impurity peaks appeared, indicating that the concentration of the dopant has no effect on crystalline phase purity of the products. The relative intensity between characteristic peaks at about 28.5, 33.0 47.4 and 56.3 2θ does not change clearly, which assigned to the crystal planes (1 1 1), (2 0 0), (2 2 0) and (3 1 1) respectively, suggesting that there is no preferred orientation or orientation crystal growth. The elaborated XRD pattern of the highest peak (Fig. 4b) reveals that, compared with pure ceria, the highest peak position (1 1 1) of the products exhibited an obvious shift to a lower angle after yttrium doping and reached about 28.41^0 (2θ), indicating that crystal lattice has expanded conspicuously due to the entry of yttrium into the crystal structure. At the same time the value of full width at half maximum (FWHM) located at 28.45^0 became larger, demonstrating that crystal size of samples doped by yttrium decreased.

Rietveld refinements were also carried out according to the diffraction lines by varying parameters in order to investigate the actual doping quantity and location (Fig. 2S). As is well known, in the cubic fluorite structure of cerium dioxide, each cerium is arranged in the face-centered cubic surrounded by eight oxygen elements. Meanwhile, oxygen elements occupied all of the tetrahedral positions and each oxygen element has four ligancy of cerium cations. Therefore, more oxygen vacancies would consequently emerge after yttrium enters the crystal lattice. When the amount of the dopant was changed without changing the other experimental conditions, there were significant changes in the lattice parameters. The lattice parameter value (a) changed from 5.4190 to 5.4273 Å (see the Table 1). It can be clearly seen that the lattice parameter value (a) after doping is larger than the bulk CeO_2 lattice parameter value $a = 5.4178$ Å even though the space group is still Fm-3m before and after doping. This indicates that yttrium has partially substituted cerium ions and has been introduced into the interior lattice, maintaining the ceria cubic fluorite structure instead of forming Y_2O_3-CeO_2 composite. In addition, a linear relationship could be drawn between the lattice value, (1 1 1) crystal plane peak position and amount of doping (see Fig. 5a and b). Lattice parameters clearly increased and the highest peak position decreased notably accompanied by an increasing amount of the dopant and finally reached a relative equilibrium. In other words, the amount of dopant plays a definitive role in determining ceria lattice parameters. Yttrium enters the crystal lattice and cerium ions of the crystal lattice are substituted by yttrium. Consequently, the crystal lattice would expand due to an increase in oxygen vacancy concentration with an increase in yttrium content, attributed to the fact that the ionic radius of yttrium is larger than that of cerium (1.019

and 0.97 Å, respectively). Particle sizes (D) of as-fabricated samples were also obtained by Whole Pattern Profile fitting instead of single peak refinement (Scherrer's formula). D values are randomly distributed about 10 nm after doping. The D value after doping is smaller than before doping (40 nm), and calculated results are extremely consistent with HR-TEM observations. A comparison of our results with those of previous studies [8,19,20] led to the following conclusion. Although changes in particle size resulted in crystal lattice expansion [21,22] or contraction of CeO$_2$, the effects would become weaker after yttrium doping. The type and

concentration of dopant play the role in the governing the lattice expansion or contraction of crystal parameters.

Raman technology is considered to be a very efficient and non-destructive technique for characterization of ceria nanoparticles and their derivatives. Raman spectra of as-fabricated samples under various experimental conditions are shown in Fig. 6. A strong Raman shift at ~460 cm^{-1} and a relatively weak shift at ~600 cm^{-1} can be detected. The shift at ~460 cm^{-1} can be assigned to F_{2g} vibration of the fluorite-type structure and it can be considered as the symmetric stretching mode of oxygen atoms around cerium ions,
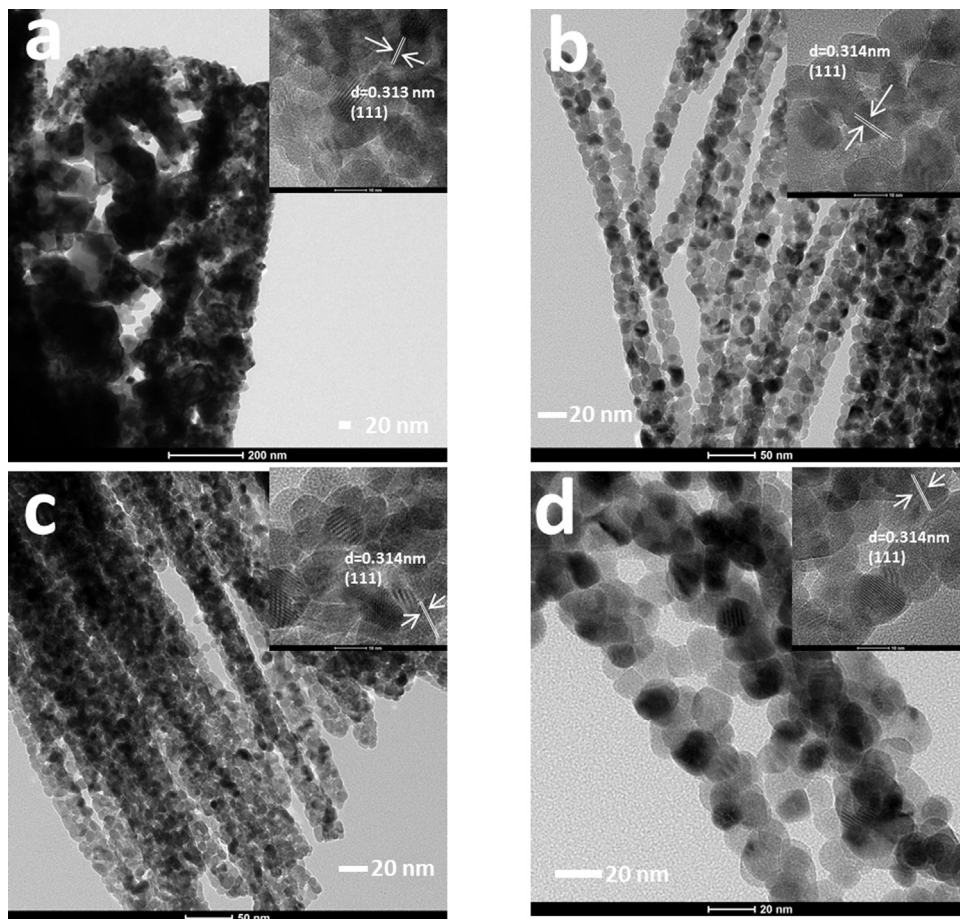

Fig. 2. HRTEM images of as-fabricated samples with different mole ratios of Ce(NO$_3$)$_3$·6H$_2$O: Y(NO$_3$)$_3$·6H$_2$O: (a) 1:0, (b) 1:0.1, (c) 1:0.2 and (d) 1:0.4.
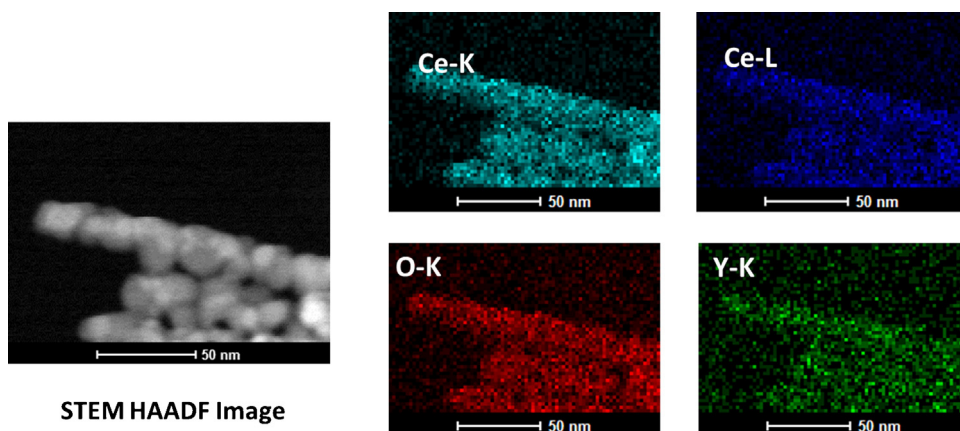

Fig. 3. HAADF image and distribution of element maps of Ce-K (skyblue), Ce-L (blue), O-K (red), and Y-K (green) after doping. (For interpretation of the references to colour in this figure legend, the reader is referred to the web version of this article.)

Table 1
Rietveld refined data from XRD patterns and oxygen vacancy value calculated by Raman spectra.

Samples/different mole ratio	Lattice parameters (a)	Calculated grain size (nm)	R_{wp}	Particles size (nm)	Area oxygen vacancies/area F_{2g} (%)
Pure CeO$_2$	5.4178	4.50	5.86	~10	6.8
1:0.05	5.4190	4.6	5.26	~10	10.9
1:0.1	5.4240	4.52	5.76	~10	11.2
1:0.2	5.4228	4.54	5.05	~10	10.2
1:0.3	5.4249	4.6	4.87	~10	10.5
1:0.4	5.4273	4.63	5.62	~10	10.3

$$PS : \frac{Area_{Oxygenvacancies}}{Area_{F_{2g}}}(\%) = \frac{\left(Area_{R_{doped}} + Area_{R_{c-o}}\right)}{Area_{F_{ag}}(\%)}$$

and the molecule retains its tetrahedral symmetry throughout. Based on the results of previous studies [23,24] and our own studies [12,13], a weak and less prominent band near ~600 cm^{-1} can be attributed to a nondegenerate longitudinal optical mode caused by a local Ce—O (R_{Ce-O}) bond symmetry stretch [25,26]. According to the results of previous studied showing that not all cerium ions show Ce^{4+} chemical valence in the lattice, small cerium ions show Ce^{3+} tervalence [27,28]. In order to maintain the particles in an electrically neutral state, the lattice oxygen would escape from the structure and finally result in the formation of intrinsic oxygen vacancies. A new and weak Raman shift at ~530 cm^{-1}, which cannot be detected in Raman spectra of pure CeO$_2$, can be seen in the inset of Fig. 6(b). It is attributed to extrinsic oxygen vacancies

caused by doping (R_{dopant}). As a dopant, yttrium enters the cubic fluorite lattice of CeO$_2$, and cerium is substituted by yttrium. In order to maintain electronic neutrality, doping cations showing different valence states with Ce^{4+} and part of the oxygen would also escape from the lattice to form extrinsic oxygen vacancies. The relativity intensities of Raman shifts of F_{2g}, R$_{dopant}$ and R$_{Ce-O}$ can be calculated from Eq. (1) [29]:

$$\frac{\text{Oxygen vacancies}}{F_{2g}} = \frac{\left(Aera_{R_{Ce-O}} + Aera_{R_{dopant}}\right)}{Aera F_{2g}} \tag{1}$$

The values are shown in Table 1, It can be seen that the value of oxygen vacancies rapidly increased at first compared with pure CeO$_2$ after yttrium doping. When the mole ratio of Ce:Y reached
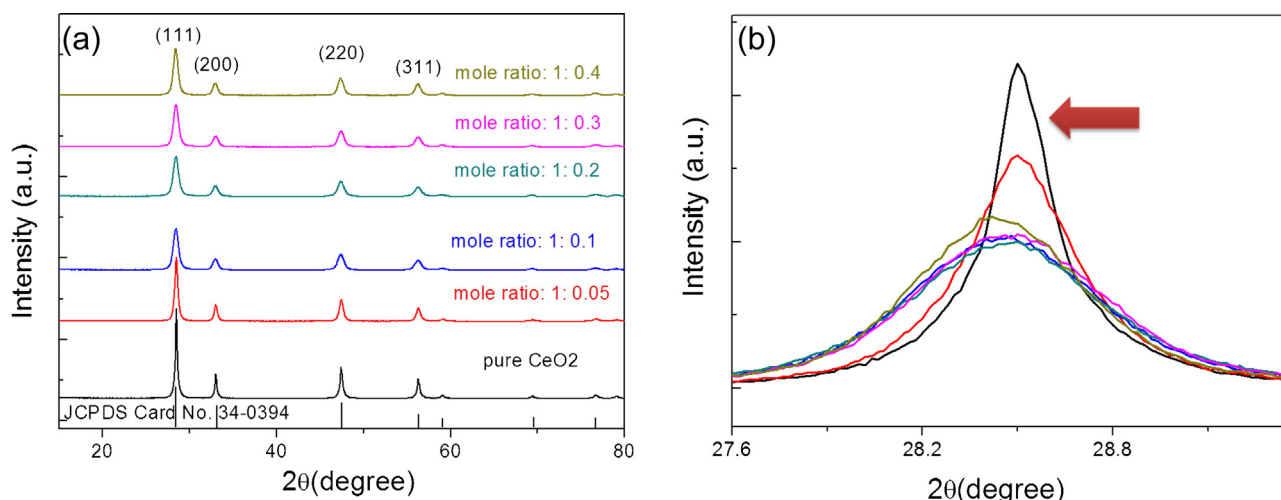

Fig. 4. XRD pattern of as-fabricated samples with different mole ratios of Ce(NO$_3$)$_3$·6H$_2$O: Y(NO3) 3·6H2O: (a) whole range and (b) elaborated XRD pattern of the highest peak (1 1 1).
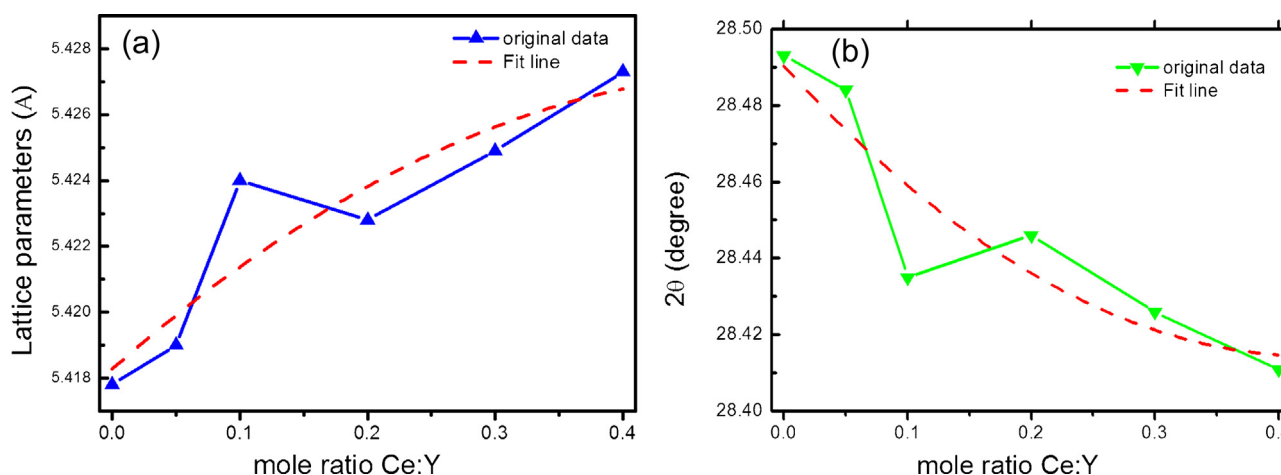

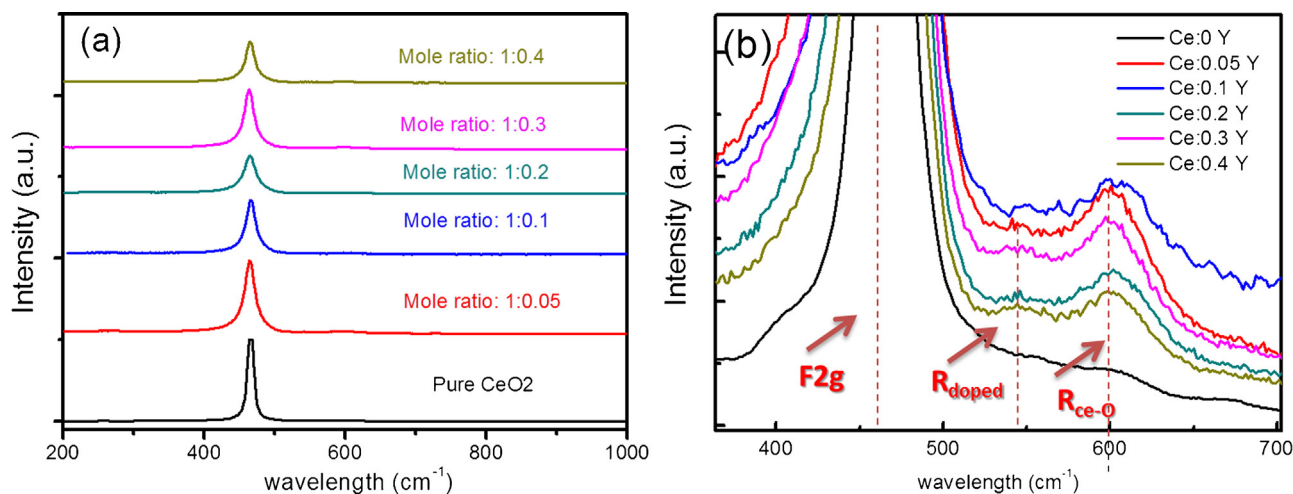**Fig. 5.** Rietveld refined data for (a) lattice parameters and (b) highest peak position as function of a dopant mole ratio.

Fig. 6. Raman spectra of as-fabricated samples with different mole ratios of $Ce(NO_3)_3 \cdot 6H_2O$: $Y(NO_3)_3 \cdot 6H_2O$: (a) whole range and (b) elaborated Raman shift.

1:0.1, the value of oxygen vacancies reached a maximum 11.2%. Finally, the value decreased and reached an approximate balance with further increase in the dopant content. The trend for change in the value can be attributed to the amount of the dopant.

At the beginning, yttrium was introduced into bulk CeO_2, and more extrinsic oxygen vacancies were obtained except intrinsic oxygen vacancies. Therefore, the value of oxygen vacancies rapidly increased. When an excessive amount of the dopants was
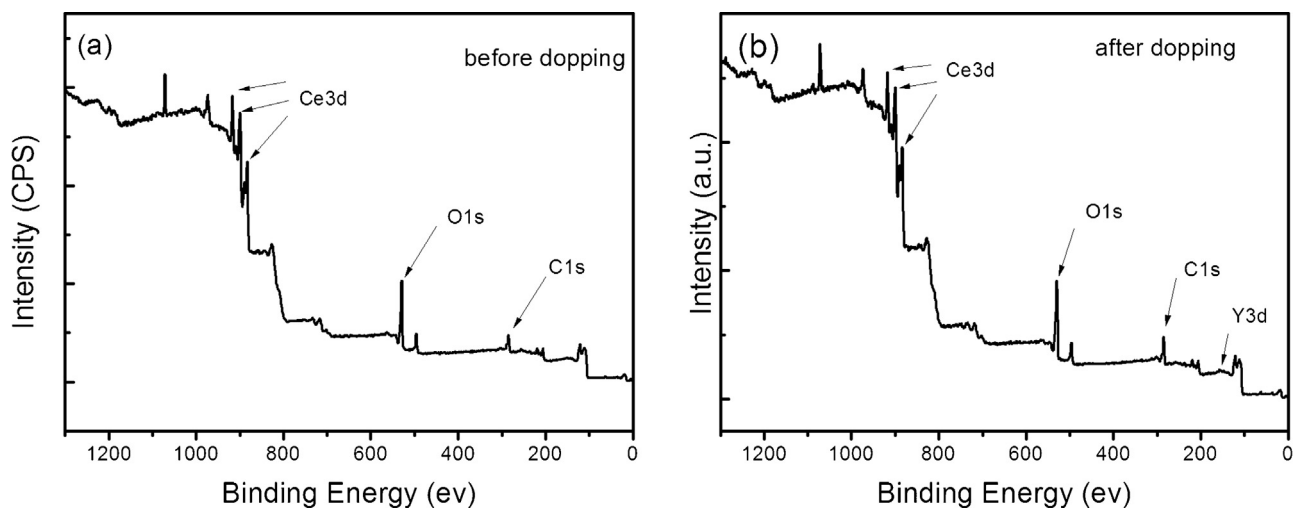

Fig. 7. Wide scanning XPS spectra of products (a) before doping and (b) after doping.
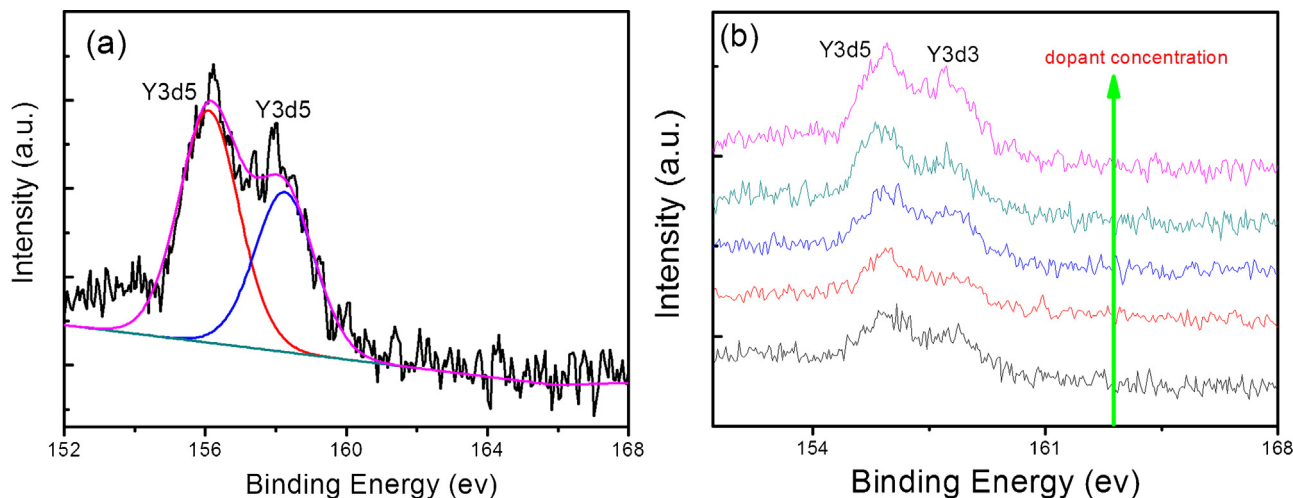

Fig. 8. High-solution XPS spectra of Y3d (a) separated peak curve and (b) different mole ratio products.

added, the oxygen vacancy concentration increased and eventually reached a steady plateau level in order to maintain electron neutrality of the system. These results of Raman analysis are consistent with the results of XPS O_{1S} analysis and activity evaluation.

3.3. X-ray photoelectron spectroscopy characterization

XPS characterization was applied to determine the CeO_2 nanoparticles before and after yttrium doping. Wide scanning XPS spectra of the product is illustrated in Fig. 7. The elements Ce, O, and C can be detected from Fig. 7(a), and they are assigned to Ce3d, O1s and C1s binding energies, respectively. Not only above elements but also yttrium element can be detected from the spectra, and it is assigned to Y3d binding energy, indicating that doping was successful (Fig. 7(b)). The elaborated Y3d XPS spectra of the products after doping are shown in Fig. 8. After deconvolution and separation, two peaks located at 156.1ev and 158.2ev, assigned to Y3d5/2 binding energy, can be founded from XPS profiles (Fig. 8(a)). Fig. 8(b) shows, after calculated these two peaks area, peak intensity and area persistent enhanced accompanied with increasing concentration dopant, indicating that more yttrium enters into the lattice of ceria with increasing dopant concentration. This result is in agreement with the results of XRD and Raman analysis.

Fig. 9 shows Ce 3d electron core level XPS spectra for as-fabricated samples and the changes in Ce 3d3/2 and Ce 3d5/2 components depending on the Ce^{3+} and Ce^{4+} oxidation states. Five pairs of doublets, (u, v), (u_1, v_1), (u_2, v_2), (u_3, v_3) and (u_0, v_0), can be decomposed from the origin region, where u and v come from Ce 3d3/2 and Ce 3d5/2 states, respectively. We observed that (u, v), (u_2, v_2) and (u_3, v_3), which were attributed to Ce 3d9 4f2 O 2p4, Ce 3d9 4f1 O 2p5 and Ce 3d9 4f0 O 2p6 final states, respectively, all belonged to the Ce^{4+} oxidation state. The two pairs doublets as (u_1, v_1) and (u_0, v_0) originated from the Ce 3d9 4f1 O 2p4 and Ce 3d9 4f1 O 2p5 final states, respectively, which correspond to the Ce^{3+} oxidation state (Fig. 9(a)). The relative amount of cerium in the tervalent oxidation state can be calculated from Eq. (2) [30]:

$$\frac{\left[Ce^{3+}\right]}{\left[Ce^{3+} + Ce^{4+}\right]} = \frac{area\left(v_0, v_1, u_0, u_1\right)}{totalarea} \quad (2)$$

Results for oxidation states are summarized in Table 2. The fitting data demonstrated that the as-fabricated samples for different dopants (Fig. 9(b)) exhibit variation of $[Ce^{3+}]$ concentration. The $[Ce^{3+}]$ concentration after doping was larger than that without doping, and when the mole ratio value reached 1:0.1, the $[Ce^{3+}]$ concentration reached a peak value of 29.76%. Then the $[Ce^{3+}]$ concentration decreased and finally reached an approximate balance.
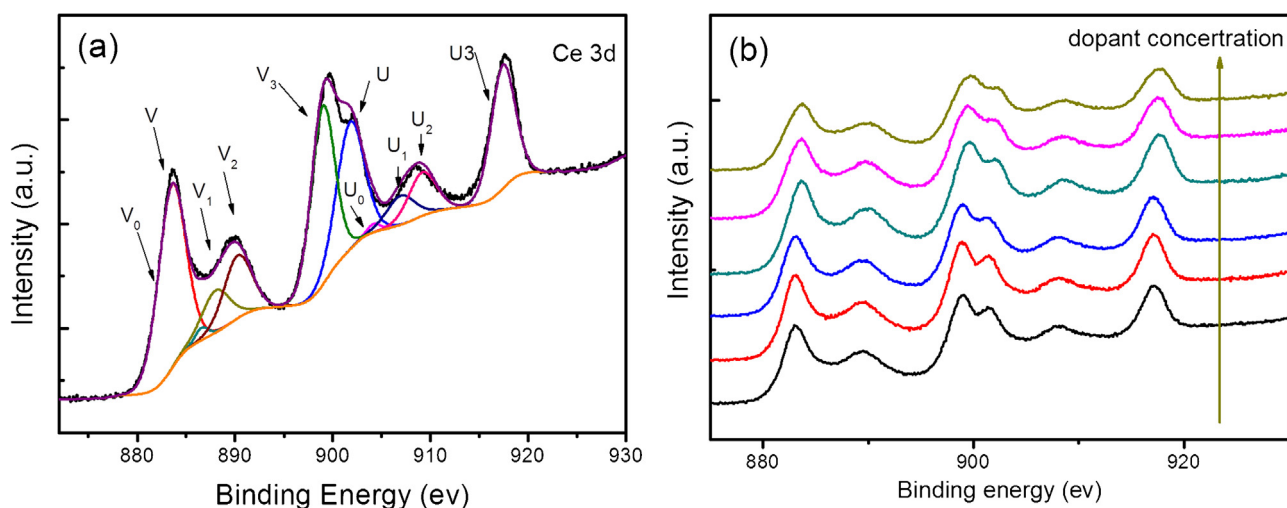

Fig. 9. High-solution XPS spectra of Ce3d (a) separated peak curve and (b) different mole ratio products.
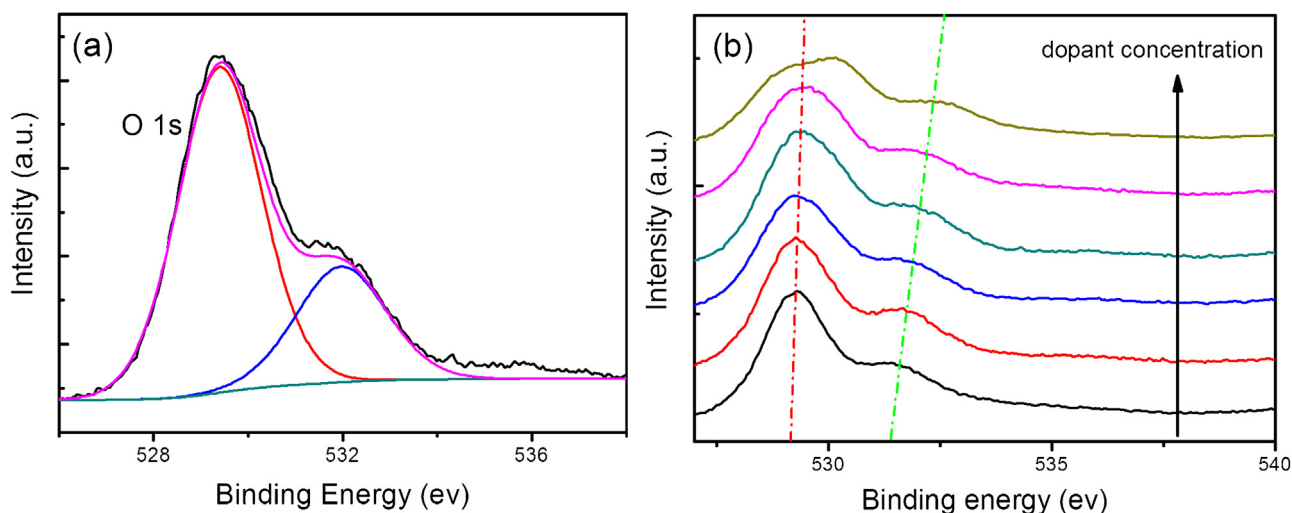

Fig. 10. High-solution XPS spectra of O1s (a) separated peak curve and (b) different mole ratio products.
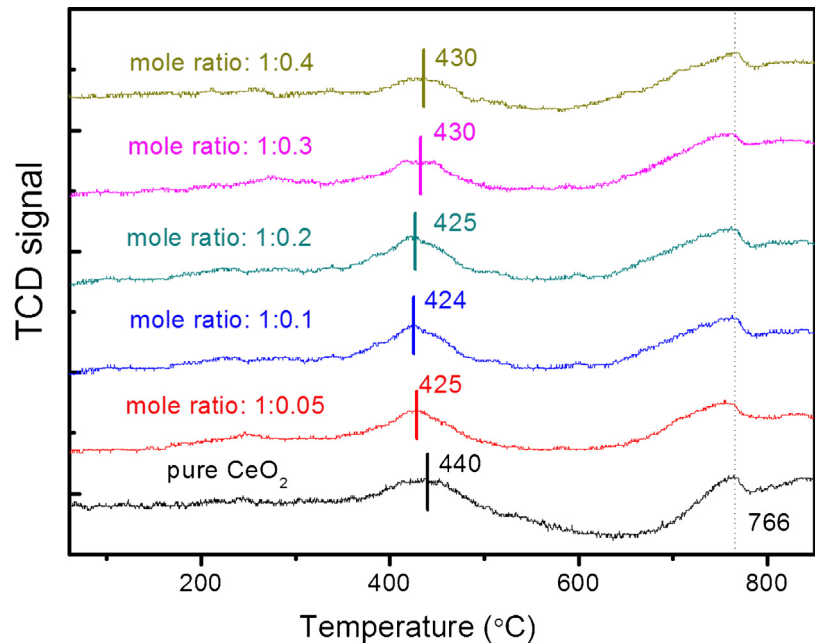
Fig. 11. H$_2$-TPR profiles of as-fabricated samples with different mole ratios of Ce(NO$_3$)$_3$·6H$_2$O: Y(NO$_3$)$_3$·6H$_2$O.
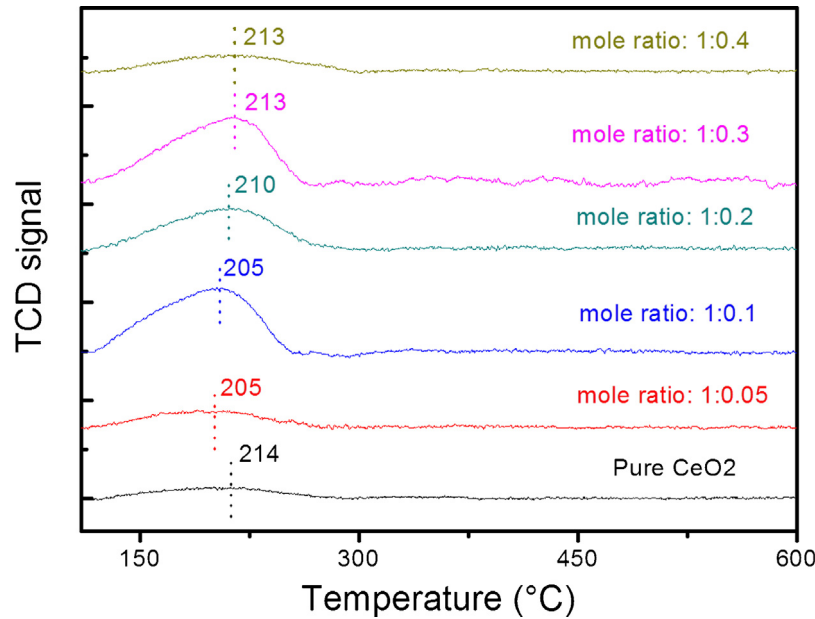

Fig. 12. O$_2$-TPD profiles of as-fabricated samples with different mole ratios of Ce(NO$_3$)$_3$·6H$_2$O: Y(NO$_3$)$_3$·6H$_2$O.

Table 2
Calculated [Ce^{3+}] and [O$_{sur}$] concentrations of as-fabricated samples from the XPS spectrum.

Sample/different mole ratio of Ce and Y	[Ce^{3+}]/[Ce^{3+}+ Ce^{4+}] %	[O$_{sur}$]/[O$_{sur}$ + O$_{lat}$] %
Pure CeO$_2$	19.0	40.5
1:0.5	25.38	52.8
1:0.1	29.76	55.8
1:0.2	23.43	52.76
1:0.3	24.00	53.59
1:0.4	23.86	53.97

$$\frac{\left[Ce^{3+}\right]}{\left[Ce^{3+} + Ce^{4+}\right]} = \frac{area\,(v_0, v_1, u_{0,} u_1)}{totalarea} \qquad \frac{[O_{sur}]}{[O_{sur} + O_{lat}]} = \frac{area\,(O_{sur})}{totalarea}$$

Fig. 10 shows O1s electron core level XPS spectra. One peak around 529.0 eV with a shoulder around 531.5 eV can be clearly seen from Fig. 10(a), and they can be attributed to lattice oxygen (O$_{lat}$) and surface active oxygen (O$_{sur}$), respectively [29,31]. Fig. 10(b) clearly demonstrates that the O$_{lat}$ and O$_{sur}$ binding energy obviously shifted to a high energy after yttrium doping, while the effects on O$_{lat}$ and O$_{sur}$ are different. The O$_{sur}$'s binding energy value shows a change of 1.2 ev from 531.3 ev to 532.5 ev with the increase in the amount of dopant. However, the O$_{lat}$'s binding energy value shows a change of 0.2 ev only from 529.33 ev to 529.53 ev. Therefore, doping of yttrium mainly affects the ceria's surface oxgyen binding energy, improving the surface oxygen binding energy and enhancing the activity of surface oxygen [32]. After deconvolution

and multiple-peak separation, we could obtain the surface oxygen ratio from the Eq. (3):

$$\frac{[O_{sur}]}{[O_{sur} + O_{lat}]} = \frac{area\,(O_{sur})}{total\,area} \qquad (3)$$

Results for surface active oxygen are summarized in Table 2A trend similar to that for the variation of $[Ce^{3+}]$ concentration can be seen. The $[O_{sur}]$ concentration after doping is larger than that without doping, and the maximum value of surface oxygen ratio is approximately 55.8% when the mole ratio value is 1:0.1. This value is higher than the others. In the following process, the $[O_{sur}]$ concentration would reach an approximate equilibrium, although the amount of yttrium is increasing.

The $[Ce^{3+}]$ and $[O_{sur}]$ concentrations value of the products can directly reflect the amount and active of oxygen vacancies and suggest that yttrium-doped CeO_2 with a porous broom-like structure should have higher catalytic activity [49].This result is well consistent with the results of H_2-TPR,O_2-TPD characterization and Raman analysis.

3.4. H_2-TPR characterization

Hydrogen temperature-programmed reduction (H_2-TPR) in a flow of hydrogen up to 900 °C was used to characterize the catalysts and probe redox properties. Fig. 11 shows H_2-TPR traces of as-fabricated samples before and after doping. In the temperature range of 50–900 °C, pure CeO_2 shows two notable reduction peaks at about 440 °C and 766 °C, respectively. The lower temperature reduction peak could be attributed to reduction of surface active oxygen of ceria, while the peak at a higher temperature could be assigned to reduction of lattice oxygen of ceria [33,34,39]. The relatively moderate shift (~10 °C) of the main reduction peak after yttrium doping to a low temperature (ca. 425 °C), relative to the profile of pure ceria, implies that the reducibility of the sample fabricated have been considerably enhanced, because the surface active oxygen reducibility is improved after yttrium doping. A trend for enhancement of reduction ability accompanied by variation of yttrium doping concentration can be clearly seen in the H_2-TPR profiles. First, the reduction peak shifts to a low temperature from 425 to 424 °C with increase in the concentration of the dopant at a low mole ratio (below 1:0.1). When the mole ratio is 1:0.1, the

reduction temperature is lowest (424 °C). With further increase in the concentration of the dopant (up to mole ratio 1:0.1), the reduction peak draw back slightly to 430 °C. Despite increase in reduction temperature, this value is still lower than that of pure ceria (440 °C). However, the reduction peak positions of lattice oxygen of ceria do not show a significant difference before and after doping and are located stably at about 766 °C, indicating that yttrium doping mainly affected the surface oxygen active spices rather than lattice oxygen. These phenomena suggest that yttrium-doped ceria with a porous broom-like structure has predominant catalytic properties, attributing to a certain amount of yttrium would increase the concentration of surface active oxygen and promote surface active oxygen reducibility.

3.5. O_2-TPD characterization

According to previous reports, surface active oxygen species such as O_2^- and O^- desorbed around 250 °C, whereas lattice oxygen from CeO_2 desorbs at a relatively higher temperature [35,36,39]. Fig. 12 shows O_2-TPD profiles before and after yttrium doping CeO_2 with a porous broom-like hierarchical structure. The oxygen desorption peak of pure ceria with a porous broom-like hierarchical structure located at about 214 °C, assigned to surface oxygen species, is lower than that of traditional CeO_2 with a 1D or 2D structure [37–39]. After yttrium doping, oxygen desorption peak shifted to a lower temperature. When the mole ratios were 1:0.05 and 1:0.1, respectively, the oxygen desorption peak was located at around 205 °C and achieved the lowest desorption temperature. In addition, on the basis of the O_2-TPD peak area, the total oxygen desorption amount reached a maximum when mole ratio was 1:0.1. With a further increase in the concentration of yttrium, the oxygen desorption peak decreased to 213 °C. Meanwhile, the total oxygen desorption amount decreased and finally reached an approximate balance. All results indicated that the activity and amount of surface active oxygen species are influenced by the dopant and morphology. Doping of a low concentration of yttrium is effective for improving the activity and amount of surface oxygen distinctly, resulting in an improvement in the catalytic performance. However, excessive concentration of yttrium doping is not effective for improving the activity and amount of surface oxygen and will restrict enhancement of the catalytic properties of the products.
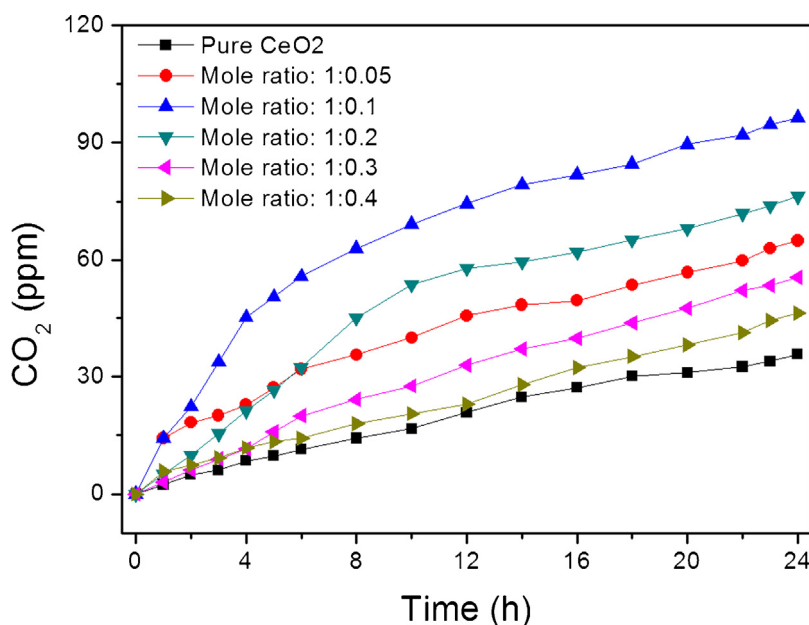

Fig. 13. Time course of CO_2 liberation from acetaldehyde decomposition of as-fabricated samples.

3.6. Photocatalytic activity for acetaldehyde decomposition

The photocatalytic activities of as-fabricated products were evaluated by measuring CO_2 evolution form the photocatalytic decomposition of acetaldehyde.

Fig. 13 shows the time course of CO_2 liberation of samples with different of dopant concentrations. Compared with pure CeO_2, photocatalytic activities were enhanced after yttrium doped. When dopant concentration is low (mole ratio <1:0.1), the as-fabricated samples show an increasing CO_2 liberation rate as in the case of pure CeO_2. When mole ratio was 1:0.1, the CO_2 liberation rate reached a maximum value. Meanwhile the yield amount of CO_2 achieved about 100 ppm. This value is three times concentration of CO_2 liberation pure ceria. Further increasing concentration of dopant (mole ratio >1:0.1), the CO_2 liberation rate decreased. This phenomenon demonstrates that a certain content dopant is beneficial for enhancement of photocatalytic activities. That's because there are high concentration of oxygen vacancies and surface active oxygen species after doped which play the predominant role in governing the trend of photocatalytic activities. According to above discussion, more surface active oxygen and oxygen vacancy exist on the surface of the broom-like ceria with porous structure. The surface oxygen vacancy can interact strongly with activity oxygen molecules to form $O_2 \cdot$ [40,41]. $O_2 \cdot$ is an efficient electron capture, which can easily trap photo-generated electrons to restrict the recombination of photogenerated electrons and holes. The formation of $O_2 \cdot$ is considered to be very important for photocatalytic decomposition of acetaldehyde. Herein, more surface oxygen and oxygen vacancy give the rise to the formation of $O_2 \cdot$, resulting in the improvement of photocatalytic activity of products. Therefore oxygen vacancies and surface active oxygen species after doped play the predominant role in governing the trend of photocatalytic activities.

4. Conclusion

In summary, CeO_2 with an yttrium-doped porous broom-like hierarchical architecture was successfully prepared by a simple hydrothermal method. The method of synthetic is effective and reproducible and can be expanded to fabrication of other rare-earth-doped morphology-controlled inorganic nanoparticle materials. The optimum doping concentration for products were found to be amole ratio of $Ce(NO_3)_3$ and $Y(NO_3)_3$ of 1:0.1. High-resolution TEM showed that yttrium-doped CeO_2 with a broom-like shape is comprised of many small particles with a crystallite size of 10 nm and porous construction can be discovered among the small particles. The present work showed that porous broom-like yttrium-doped CeO_2 exhibits an advantage of photocatalytic activity. The results of photocatalytic activity evaluation were consistent with the results of Raman, XPS, XRD and SEM analyses. The trend for changes in photocatalytic activity was explained by the oxygen vacancies and surface active oxygen species derived from changing yttrium doping. Consequently, yttrium-doped porous broom-like hierarchical CeO_2 is a promising material for practical applications in catalytic materials as well as other novel environmental friendly materials.

Acknowledgements

Appendix A. Supplementary data

Supplementary data associated with this article can be found, in the online version, at http://dx.doi.org/10.1016/j.apcatb.2015.10.021.

References

[1] K. Zhou, Z. Yang, S. Yang, Chem. Mater. 19 (2007) 1215–1217.
[2] H. Imagawa, A. Suda, K. Yamamura, S. Sun, J. Phys. Chem. C 115 (2011) 1740–1745.
[3] L. Yan, R. Yu, J. Chen, X. Xing, Cryst. Growth Des. 8 (2008) 1474–1477.
[4] R.K. Pati, I.C. Lee, K.J. Gaskell, S.H. Ehrman, Langmuir 25 (2008) 67–70.
[5] Z.-L. Wang, G.-R. Li, Y.-N. Ou, Z.-P. Feng, D.-L. Qu, Y.-X. Tong, J. Phys. Chem. C 115 (2010) 351–356.
[6] Z. Wang, Z. Quan, J. Lin, Inorg. Chem. 46 (2007) 5237–5242.
[7] S. Kitano, N. Murakami, T. Ohno, Y. Mitani, Y. Nosaka, H. Asakura, K. Teramura, T. Tanaka, H. Tada, K. Hashimoto, H. Kominami, J. Phys. Chem. C 117 (2013) 11008–11016.
[8] C. Paun, O.V. Safonova, J. Szlachetko, P.M. Abdala, M. Nachtegaal, J. Sa, E. Kleymenov, A. Cervellino, F. Krumeich, J.A. van Bokhoven, J. Phys. Chem. C 116 (2012) 7312–7317.
[9] M. Jobbágy, F. Mariño, B. Schönbrod, G. Baronetti, M. Laborde, Chem. Mater. 18 (2006) 1945–1950.
[10] H. Xiao, Z. Ai, L. Zhang, J. Phys. Chem. C 113 (2009) 16625–16630.
[11] F. Dvořáík, O. Stetsovych, M. Steger, E. Cherradi, I. Matoliínovaí, N. Tsud, M. Škoda, T. Skaíla, J. Mysliveček, V. Matoliín, J. Phys. Chem. C 115 (2011) 7496–7503.
[12] B. Xu, Q. Zhang, S. Yuan, M. Zhang, T. Ohno, Chem. Eng. J. 260 (2015) 126–132.
[13] B. Xu, Q. Zhang, S. Yuan, M. Zhang, T. Ohno, Appl. Catal. B: Environ. 164 (2015) 120–127.
[14] Z. Yang, D. Han, D. Ma, H. Liang, L. Liu, Y. Yang, Cryst. Growth Des. 10 (2009) 291–295.
[15] L.-W. Qian, X. Wang, H.-G. Zheng, Cryst. Growth Des. 12 (2011) 271–280.
[16] S.L. Mitchell, J. Guzman, Mater. Chem. Phys. 114 (2009) 462–466.
[17] L.-S. Zhong, J.-S. Hu, A.-M. Cao, Q. Liu, W.-G. Song, L.-J. Wan, Chem. Mater. 19 (2007) 1648–1655.
[18] Z.-Y. Pu, X.-S. Liu, A.-P. Jia, Y.-L. Xie, J.-Q. Lu, M.-F. Luo, J. Phys. Chem. C 112 (2008) 15045–15051.
[19] A.E. Baranchikov, O.S. Polezhaeva, V.K. Ivanov, Y.D. Tretyakov, CrystEngComm 12 (2010) 3531.
[20] C.-Y. Cao, Z.-M. Cui, C.-Q. Chen, W.-G. Song, W. Cai, J. Phys. Chem. C 114 (2010) 9865–9870.
[21] F. Zhang, S.-W. Chan, J.E. Spanier, E. Apak, Q. Jin, R.D. Robinson, I.P. Herman, Cerium oxide nanoparticles: size-selective formation and structure analysis, Appl. Phys. Lett. 80 (2002) 127.
[22] X.D. Zhou, W. Huebner, Appl. Phys. Lett. 79 (2001) 3512.
[23] Y. Lee, G. He, A.J. Akey, R. Si, M. Flytzani-Stephanopoulos, I.P. Herman, J. Am. Chem. Soc. 133 (2011) 12952–12955.
[24] S. Chang, M. Li, Q. Hua, L. Zhang, Y. Ma, B. Ye, W. Huang, J. Catal. 293 (2012) 195–204.
[25] Z.D. Dohčević-Mitrovi, M. Grujić-Brojčin, M. Šćepanović, Z.V. Popović, S. Bošković, B. Matović, M. Zinkevich, F. Aldinger, Condens. Matter 18 (2006) S2061–S2068.
[26] K.C.H.J.R. McBride, B.D. Poindexter, W.H. Weber, J. Appl. Phys. 76 (1994) 2435.
[27] Y. Lee, G. He, A.J. Akey, R. Si, M. Flytzani-Stephanopoulos, I.P. Herman, J. Am. Chem. Soc. 133 (2011) 12952–12955.
[28] S. Chang, M. Li, Q. Hua, L. Zhang, Y. Ma, B. Ye, W. Huang, J. Catal. 293 (2012) 195–204.
[29] L. Ma, D. Wang, J. Li, B. Bai, L. Fu, Y. Li, Appl. Catal. B Environ. 148–149 (2014) 36–43.
[30] Y.V.f Holger Borchert, Vasiliy V. Kaichev, Igor P. Prosvirin, J. Phys. Chem. B 109 (2005) 5728–5738.
[31] Benjaram M. Reddy, Ataullah Khan, J. Phys. Chem. B 106 (2002) 10964–10972.
[32] C. Ho, J. Yu, T. Kwong, A. Mak, S. Lai, Chem. Mater. 17 (2005) 4514–4522.
[33] Karl Sohlberg, Sokrates T. Pantelides, Stephen J. Pennycook, J. Am. Chem. Soc. 123 (2001) 6609–6611.
[34] M. Jobbaígy, F. Marin˜o, B. Schönbrod, G. Baronetti, M. Laborde, Chem. Mater. 18 (2006) 1945–1950.
[35] G. Avgouropoulos, T. Ioannides, J. Mol. Catal. A: Chem. 296 (2008) 47–53.
[36] M. Li, Z. Wu, S.H. Overbury, J. Catal. 306 (2013) 164–176.
[37] Sanjaya D. Senanayake, David R. Mullins, J. Phys. Chem. C 112 (2008) 9744–9752.
[38] Matthew B. Boucher, Nan Yi, Forrest Gittleson, Branko Zugic, Howard Saltsburg, Maria Flytzani-Stephanopoulos, J. Phys. Chem. C 115 (2011) 1261–1268.
[39] Tana M. zhang, J. li, H. Li, Y. li, W. Shen, Catal. Today 148 (2009) 179–183.
[40] S.A. Bilms, P. Mandelbaum, F. Alvarez, J. Phys. Chem. B 104 (2000) 9851–9858.
[41] I. Ait-Ichou, M. Formenti, B. Pommier, S.J. Teichner, J. Catal. 91 (1985) 293–307.